Ni−In Synergy in CO2 Hydrogenation to Methanol

Jiadong Zhu, Francesco Cannizzaro, Liang Liu, Hao Zhang, Nikolay Kosinov, Ivo. A. W. Filot, Jabor Rabeah, Angelika Brückner, and Emiel J. M. Hensen*

ACCESS | Metrics & More | Article Recommendations | Supporting Information

ABSTRACT: Indium oxide (In_2O_3) is a promising catalyst for selective CH_3OH synthesis from CO_2 but displays insufficient activity at low reaction temperatures. By screening a range of promoters (Co, Ni, Cu, and Pd) in combination with In_2O_3 using flame spray pyrolysis (FSP) synthesis, Ni is identified as the most suitable first-row transition-metal promoter with similar performance as Pd−In_2O_3. $NiO−In_2O_3$ was optimized by varying the Ni/In ratio using FSP. The resulting catalysts including In_2O_3 and NiO end members have similar high specific surface areas and morphology. The main products of CO_2 hydrogenation are CH_3OH and CO with CH_4 being only observed at high NiO loading (≥ 75 wt %). The highest CH_3OH rate (~ 0.25 $g_{MeOH}/(g_{cat}$ h), 250 °C, and 30 bar) is obtained for a NiO loading of 6 wt %. Characterization of the as-prepared catalysts reveals a strong interaction between Ni cations and In_2O_3 at low NiO loading (≤ 6 wt %). H_2-TPR points to a higher surface density of oxygen vacancy (O_v) due to Ni substitution. X-ray photoelectron spectroscopy, X-ray absorption spectroscopy, and electron paramagnetic resonance analysis of the used catalysts suggest that Ni cations can be reduced to Ni as single atoms and very small clusters during CO_2 hydrogenation. Supportive density functional theory calculations indicate that Ni promotion of CH_3OH synthesis from CO_2 is mainly due to low-barrier H_2 dissociation on the reduced Ni surface species, facilitating hydrogenation of adsorbed CO_2 on O_v.

KEYWORDS: CO_2 hydrogenation, CH_3OH, flame spray pyrolysis, Ni promotion, Ni−In synergy
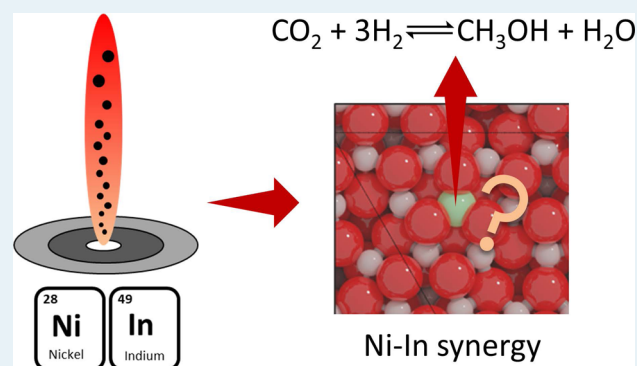
1. INTRODUCTION

The large amounts of CO_2 released into the atmosphere, mainly by the combustion of fossil fuels, constitute a significant threat to human well-being because it can lead to severe climate changes including global warming, sea-level rise, and ocean acidification.[1−3] A promising solution is to capture CO_2 from combustion processes or directly from air for reuse in fuels and chemicals. This can for instance be achieved by catalytic hydrogenation of CO_2 with H_2 generated from renewable energy sources such as solar and wind.[4−7] This carbon capture and use (CCU) approach has the advantage over carbon capture and storage (CCS) that carbon is used in a circular manner, eventually leading to the replacement of fossil fuels by renewable resources for covering the energy demand. Besides sustainable energy carriers, hydrogenation of CO_2 can be used to obtain important intermediates for the chemical industry. Methanol is particularly attractive in the overall context of sustainability because it can be directly used as a fuel or be converted to a wide range of chemicals such as formaldehyde, dimethyl ether, olefins, hydrocarbon fuels, etc.[8−10]

The $Cu/ZnO/Al_2O_3$ catalysts used in the current commercial methanol synthesis process were pioneered by Imperial Chemical Industries in the 1960s.[11,12] These catalysts are optimized for the conversion of synthesis gas (a mixture of mainly CO/H_2). Challenges arise however in the hydrogenation of CO_2 to CH_3OH. The high activity of the Cu−ZnO-based catalysts in the reverse water gas shift (rWGS) reaction decreases the CH_3OH selectivity.[13] Moreover, deactivation of the Cu−ZnO-based catalysts is accelerated by the large amounts of water byproduct formed during CO_2 hydrogenation.[14−16] Many efforts have been made to optimize Cu-based catalysts for selective CO_2 hydrogenation to CH_3OH.[5,17] An important corollary of these studies is that tuning Cu−support interactions using other supports than alumina can mitigate some of these drawbacks. For example, zirconia (ZrO_2) has been widely investigated as a support with improved catalytic performance over alumina-supported catalysts.[18−21]

Exploring completely new catalytic formulations is another approach to develop practical catalysts for CO_2 hydrogenation to CH_3OH. Several promising materials have been reported, for instance, mixed oxides ($ZnO-ZrO_2$ and MnO_x/Co_3O_4),[22,23] molybdenum carbides,[24,25] molybdenum phosphides,[26] and intermetallic compounds ($GaPd_2$ and Ni_5Ga_3).[27,28] In recent years, oxygen-defective In_2O_3 has been proposed as an alternative catalyst for efficient CH_3OH synthesis from CO_2.[29−33] The role of oxygen vacancies in the In_2O_3 surface has been emphasized for the adsorption and hydrogenation of CO_2.[29,30] Furthermore, ZrO_2 has been extensively studied as a support for In_2O_3 due to the synergistic interactions between these two components.[34−39] Pérez-Ramirez's group reported that nanosizing In_2O_3 by dispersion over ZrO_2 can substantially enhance CH_3OH synthesis from CO_2.[39] Addition of Pd was also found to significantly promote In_2O_3 for CO_2 hydrogenation to CH_3OH.[40−44] It was proposed that low-nuclearity Pd clusters stabilized by a Pd-doped In_2O_3 surface can enhance H_2 activation and, therefore, CH_3OH productivity.[43]

Given its price, it would be advantageous to replace Pd by a more earth-abundant metal. Earlier investigations have shown that the activity of In_2O_3 for CO_2-to-CH_3OH conversion can be promoted by Co and Cu.[45−47] The replacement of Pd by Ni, a typical methanation catalyst, has been studied as well. Richard and Fan, for instance, found that $NiInAl/SiO_2$ catalysts derived from phyllosilicate precursors can catalyze CO_2 hydrogenation to CH_3OH at ambient pressure although with low selectivity (<4%).[48] In another study, Snider et al. suggested that the higher activity of bimetallic Ni−In catalysts for CH_3OH synthesis from CO_2 in comparison to In_2O_3 is related to the synergistic interactions between a Ni−In alloy and In_2O_3.[42] Using wet chemical reduction with sodium borohydride, Jia et al. observed a similar promoting effect of Ni on In_2O_3 for CO_2 hydrogenation to CH_3OH. They suggested that the Ni promotion is associated with highly dispersed Ni species in strong interaction with In_2O_3.[49] In a recent report, Frei et al. studied Ni-promoted In_2O_3 in detail for CO_2 hydrogenation, highlighting the formation of highly dispersed $InNi_3$ layers on In_2O_3.[50]

In the present study, a series of $NiO-In_2O_3$ catalysts were investigated to further understand the Ni promotion on In_2O_3 for CO_2 hydrogenation to CH_3OH. For this purpose, a one-step FSP method[51,52] was used to synthesize well-defined NiO-In_2O_3 catalysts with controlled Ni−In interactions. Catalytic activity measurements at 250 °C and 30 bar point to a significant synergy between Ni and In_2O_3 for CH_3OH synthesis from CO_2: small amounts of Ni lead to substantially increased CH_3OH formation rates, while high Ni loadings result in CH_4 formation. To elucidate the Ni−In synergy, various techniques including N_2 physisorption, transmission electron microscopy (TEM), X-ray diffraction (XRD), electron paramagnetic resonance (EPR), H_2-TPR, X-ray photoelectron spectroscopy (XPS), and X-ray absorption spectroscopy (XAS) were employed to characterize the as-prepared and used NiO-In_2O_3 catalysts, and density functional theory calculations were carried out to unravel the role of different Ni species in H_2 activation.

2. EXPERIMENTAL SECTION

2.1. Catalyst Preparation. A series of metal (M = Co, Cu, Ni, and Pd with loading of 5 wt %)-promoted In_2O_3 catalysts were prepared by a one-step FSP method using a Tethis

NPS10 setup. Typically, a precursor solution was prepared by dissolving appropriate amounts of $In(NO_3)_3 \cdot xH_2O$ (99%, Alfa Aesar) and metal precursor ($Co(NO_3)_2 \cdot 6H_2O$ (98%, Sigma Aldrich), $Cu(NO_3)_2 \cdot 3H_2O$ (99.5%, Sigma Aldrich), Ni-$(NO_3)_2 \cdot 6H_2O$ (98.5%, Sigma Aldrich), and $Pd(OCOCH_3)_2$ (98%, Sigma Aldrich)) in a 1:1 (vol %) solvent mixture of ethanol (HPLC, Sigma Aldrich) and 2-ethylhexanoic acid (99%, Sigma Aldrich) at room temperature to a total metal concentration (In + M) of 0.15 M. The catalyst preparation was started by injecting the precursor solution into the nozzle of the flame synthesis setup at a flow rate of 5 mL/min. The flame was fed with a 1.5 L/min methane and 3.0 L/min oxygen flow with an additional 5.0 L/min oxygen dispersion flow around it. The catalyst powder was collected from the quartz filter placed downstream of the flame region. The as-prepared catalysts are denoted M-In_2O_3. Another series of catalysts were prepared using the same procedure to study the Ni promoter in detail. The as-prepared Ni−In catalysts are denoted In_2O_3, $NiO(x)-In_2O_3$, and NiO, where x stands for NiO loading in the catalysts (wt %).

2.2. Catalyst Characterization. *2.2.1. N_2 Physisorption.* The textural properties of the as-prepared and used catalysts were studied by N_2 physisorption at −196 °C using a Micrometrics TriStar II 3020 instrument. For this purpose, approximately 100 mg of samples was transferred into glass sample tubes and pretreated at 120 °C under a nitrogen flow overnight before the measurements. The Brunauer−Emmett−Teller (BET) method was used to calculate the specific surface area of the catalysts.

2.2.2. Transmission Electron Microscopy (TEM). The morphology of the as-prepared and used catalysts was studied by TEM using a FEI Tecnai (type Sphera) instrument operating at an acceleration voltage of 200 kV. For sample preparation, appropriate amounts of samples were dispersed in ethanol under ultrasonic exposure and deposited on holey Cu grids.

2.2.3. X-ray Diffraction (XRD). The crystal structure of the as-prepared catalysts was analyzed using a Bruker D2 Phaser diffractometer with Cu Kα radiation (1.5406 Å). The XRD patterns were recorded between 15 and 80° with a step size of 0.05° at a 1.0 s/step scan rate.

2.2.4. Electron Paramagnetic Resonance (EPR) Spectroscopy. In situ EPR spectra of selected NiO-In_2O_3 catalysts during CO_2 hydrogenation were measured at ambient pressure using an X-band EPR EMX CW-micro spectrometer (Bruker) with a microwave power of Ca 6.9 mW and modulation frequency and amplitude of 100 kHz and 5 G, respectively, while ex situ EPR spectra were recorded on an X-band EPR EMX CW-micro spectrometer (Bruker). For monitoring the EPR spectra at low temperature, the EPR spectrometer was equipped with a temperature controller and liquid N_2 cryostat. The effective g values (g_{eff}) were calculated using eq 1, where h and β denote Planck's constant and the Bohr magneton constant, respectively, and ν and B_0 represent, respectively, the frequency and the magnetic resonance field.

$$h\nu = g_{eff}\beta B_0 \tag{1}$$

2.2.5. Temperature-Programmed Reduction (H_2-TPR). The reducibility of the as-prepared catalysts was analyzed by H_2-TPR using a Micromeritics AutoChem II setup. Typically, about 50 mg of sample was loaded into a quartz U-tube between two quartz wool layers. The sample was pretreated at 200 °C for 1 h in a 5 vol % O_2 in a He flow of 50 mL/min

before the measurements. The TPR profile was recorded by heating the sample from 40 to 700 °C at the rate of 10 °C/min in a 4 vol % H_2 in a He flow of 50 mL/min. The H_2 consumption was monitored by a thermal conductivity detector (TCD) and calibrated against a reference Cu/SiO$_2$ sample.

2.2.6. X-ray Photoelectron Spectroscopy (XPS). The surface chemical properties of the as-prepared and used catalysts after CO_2 hydrogenation were studied using a K-Alpha XPS instrument (Thermo Scientific) with a monochromatic small-spot X-ray source and a 180° double-focusing hemispherical analyzer. For the analysis of used catalysts, a quasi-in situ approach was adopted. Specifically, the samples were placed on a double-sided carbon tape in a glovebox and transferred to the spectrometer via an airtight transfer holder. The sample preparation of the as-prepared catalysts was carried out at ambient conditions. Spectra were collected using an aluminum anode (Al Kα = 1486.68 eV) operating at 72 W and a spot size of 400 μm. Survey scans were measured at a constant pass energy of 200 eV and region scans at 50 eV. The spectra were analyzed using CasaXPS software (version 3.2.23), and energy calibration was performed again the C 1s peak of adventitious carbon at a binding energy of 284.6 eV.

2.2.7. X-ray Absorption Spectroscopy (XAS). Extended X-ray absorption fine structure (EXAFS) measurements at the Ni K-edge and In K-edge were performed at beamline B18 of the Diamond Light Source (Didcot, UK). EXAFS measurements of the as-prepared and used catalysts were performed in the fluorescence mode with a 36-element Ge detector. Notably, the used samples were prepared and sealed using Kapton tapes in a glovebox, and the as-prepared samples were prepared at ambient conditions. The NiO reference was measured in the transmission mode. Metallic Ni and In foils were measured simultaneously with each sample in the transmission mode for energy calibration. Si(111) and Si(311) monochromators were used at Ni and In K-edges, respectively. EXAFS data reduction includes energy calibration, background subtraction, and normalization, and EXAFS fitting analysis was carried out using the Demeter package (Athena/Artemis software).[53] Scattering paths were calculated using the FEFF6 code based on crystal structures of NiO, Ni metal, and In$_2$O$_3$. A Ni–In single scattering path was also included for the EXAFS fitting. In a typical fitting procedure, the energy shift (E_0), distance change (ΔR), coordination number (CN), and Debye–Waller factor (σ^2) were fitted, whereas the amplitude reduction factors (S_0^2) were determined from the EXAFS fitting of the NiO reference and the as-prepared In$_2$O$_3$ sample. The amplitude reduction factors were fixed while fitting other parameters. The plotted Fourier transformed EXAFS results weighted by k^3 have not been phase-corrected.

2.3. Catalytic Activity Measurements. The catalytic performance of the as-prepared catalysts in CO_2 hydrogenation was evaluated at 250 °C and 30 bar using a down-flow stainless steel reactor (ID = 4 mm). Typically, about 50 mg of sieved catalyst (125–250 μm), diluted with 200 mg of SiC, was loaded into the reactor and pretreated at 250 °C (rate = 5 °C/min) and 1 bar for 1 h in a N_2 flow of 10 mL/min. After the pretreatment, the catalyst was exposed to a reaction mixture flow (CO_2/H_2/N_2 = 10:30:10 mL/min), and the pressure in the reactor was increased to 30 bar using a back-pressure regulator. The effluent gas mixture was continuously analyzed by an online gas chromatograph (Interscience, CompactGC) equipped with Rtx-1 (FID), Rt-QBond and Molsieve 5A

(TCD), and Rt-QBond (TCD) columns. Catalytic measurements typically lasted for ca. 12 h until steady-state was reached. CO_2 conversion (X), product selectivity (S), and product formation rate (r) were calculated using the following equations:

$$X(CO_2)$$
$$= \frac{F(CO)_{out} + F(CH_3OH)_{out} + F(CH_4)_{out}}{F(CO_2)_{out} + F(CO)_{out} + F(CH_3OH)_{out} + F(CH_4)_{out}} \quad (2)$$

$$S(product) = \frac{F(product)_{out}}{F(CO)_{out} + F(CH_3OH)_{out} + F(CH_4)_{out}} \quad (3)$$

$$r(product) = \frac{F(product)_{out}}{V_m \times m_{cat}} \quad (4)$$

where F stands for the volumetric flow rate calculated based on the N_2 internal standard using calibrated response factors and V_m is the molar volume of ideal gas at standard conditions. For the XPS and XAS analyses of the used catalysts, the catalysts after catalytic tests were transferred without air exposure: the reactor was depressurized at 250 °C, cooled to room temperature in a N_2 flow of 10 mL/min, sealed with two three-way valves, and transferred to a glovebox for sample storage and preparation.

2.4. Density Functional Theory Calculations. All density functional theory (DFT) calculations were conducted using the projector augmented wave (PAW) method and the Perdew–Burke–Ernzerhof (PBE) functional as implemented in the Vienna ab initio simulation package (VASP) code.[54,55] Solutions of the Kohn–Sham equations were calculated using a plane-wave basis set with a cutoff energy of 400 eV. The semicore 5s and 5p states of In were treated explicitly as valence states within the scalar-relativistic PAW approach. The Brillouin zone was sampled using a 3 × 3 × 1 Monkhorst–Pack grid. Electron smearing was employed using Gaussian smearing with a smearing width (σ) of 0.1 eV. The stoichiometric In$_2$O$_3$(111) surface was modeled as a two-dimensional slab with periodic boundary conditions. A 20 Å vacuum region was used in the c-direction to avoid spurious interactions of adsorbed species between neighboring super cells. It was verified that the electron density approached zero at the edges of the periodic supercell in the c-direction. The supercell has a dimension of 14.57 Å × 14.57 Å × 26.01 Å. The In$_2$O$_3$(111) slab consists of 96 O atoms and 64 In atoms, distributed in four atomic layers. Three different Ni-containing models were constructed and optimized by DFT: (i) a Ni atom doped into In$_2$O$_3$(111) replacing an In atom, (ii) a Ni atom adsorbed on the In$_2$O$_3$(111) surface, and (iii) a Ni$_8$ cluster adsorbed on the In$_2$O$_3$(111) surface. The activation of H_2 on these surface models was investigated, and transition states were determined using the climbing-image nudged elastic band (CI-NEB) method.[56] A frequency analysis was performed to confirm that all transition geometries corresponded to a first-order saddle point on the potential energy surface with an imaginary frequency in the direction of the reaction coordinate.[57] The Hessian matrix was constructed using a finite difference approach with a step size of 0.0015 Å for displacement of individual atoms along each Cartesian coordinate. The corresponding normal-mode vibrations were

used to determine the zero-point energy corrections and the vibrational partition functions.

3. RESULTS AND DISCUSSION

3.1. Screening of Metal Promotion. Using the one-step FSP approach, we prepared three In_2O_3-based catalysts promoted by base metals (Co, Ni, and Cu) together with Pd-promoted and unpromoted In_2O_3 catalysts. The loading of a metal promoter in these catalysts was kept at 5 wt %. XRD analysis (Figure S1) shows that all of the diffraction peaks belong to the cubic In_2O_3 phase (PDF# 00-006-0416). The average crystallite size of the samples (estimated by the Scherrer equation) was ~9 nm, irrespective of the metal promoter. No diffraction peaks related to any promoter in metallic or oxidic forms were observed, suggesting that all of the promoter metals are highly dispersed or amorphous in the as-prepared catalysts. The M-In_2O_3 and In_2O_3 catalysts were evaluated for CO_2 hydrogenation under the conditions of 250 °C and 30 bar. The complete catalytic results are listed in Table S1. A comparison of CH_3OH formation rates is presented in Figure 1. The Co-In_2O_3 and Cu-In_2O_3 displayed
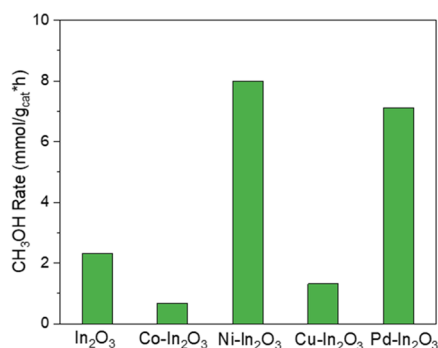
Figure 1. Metal promoter screening (M = 5 wt %) for In_2O_3 in CO_2 hydrogenation to CH_3OH. Reaction conditions: 50 mg of catalyst, 250 °C, 30 bar, and $CO_2/H_2/N_2$ = 10:30:10 mL/min.

lower CH_3OH rates than In_2O_3, while Ni and Pd additions gave rise to similar promotion in CH_3OH formation. Note, however, that due to a lower activity in the rWGS reaction, the Pd-In_2O_3 displayed a higher CH_3OH selectivity in comparison to Ni–In_2O_3 (72 vs 53%). As Pd is a relatively expensive precious metal, which has already been extensively investigated to promote In_2O_3 for CO_2 hydrogenation to CH_3OH,[40−43] we focused in this work on the development of practical In_2O_3-based catalysts for CH_3OH synthesis from CO_2 using Ni as a promoter.

3.2. Basic Characterization. The specific surface areas of the as-prepared NiO-In_2O_3 catalysts were determined by N_2 physisorption (Table 1). Clearly, all of the samples display high specific surface areas. The values of In_2O_3 and NiO samples are 123 and 137 m²/g, respectively. The binary NiO-In_2O_3 samples have slightly lower surface areas in the range of 98−114 m²/g. The morphology and particle size distribution of these catalysts were studied by TEM. Figure 2 shows that all of the samples display a similar morphology consisting of homogeneously distributed globular nanoparticles, irrespective of the vast difference in chemical composition. The as-prepared NiO-In_2O_3 catalysts have comparable average particle size, ranging from 6.5 to 7.5 nm, as estimated from the TEM measurements.

Table 1. Specific Surface Area and In_2O_3 Lattice Constant of the As-Prepared NiO-In_2O_3 Catalysts

catalyst	S_{BET} (m²/g)	In_2O_3 lattice constant a (Å)
In_2O_3	123	10.118
NiO(1)-In_2O_3	110	10.112
NiO(6)-In_2O_3	98	10.110
NiO(25)-In_2O_3	104	n.a.
NiO(50)-In_2O_3	110	n.a.
NiO(75)-In_2O_3	114	n.a.
NiO	137	n.a.

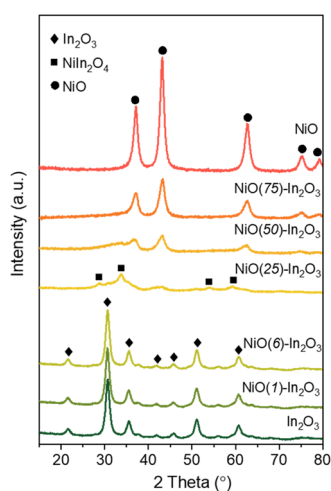XRD patterns of the as-prepared NiO-In_2O_3 catalysts are shown in Figure 3. Samples with a NiO loading up to 6 wt % have the cubic crystal structure of In_2O_3 (PDF# 00-006-0416). In addition, the In_2O_3 lattice constant estimated from the Rietveld refinement decreases with increasing NiO loading (Table 1), implying the substitution of Ni cations for the larger In cations in In_2O_3. It should be noted however that the changes in the lattice constant are very small. The sample with an intermediate NiO loading of 25 wt % displays new diffraction peaks, which are likely due to a $NiIn_2O_4$ spinel phase.[58−60] Samples with NiO loading of 50 wt % and higher mainly consist of the NiO phase (PDF# 00-047-1049). The significant broadening of all of the diffraction peaks points to the nanocrystalline nature of the as-prepared NiO-In_2O_3 catalysts, in line with the previous N_2 physisoprtion and TEM results.

3.3. Catalytic Activity Measurements. The CO_2 hydrogenation performance of the as-prepared NiO-In_2O_3 catalysts was determined at 250 °C and 30 bar. Figure 4a shows that addition of a small amount of NiO (x = 1 and 6) leads to a substantial increase of CO_2 conversion. Nevertheless, the product distribution remains nearly unchanged with CH_3OH and CO as the main products, implying that the active sites for CO_2 activation in these catalysts (x = 1 and 6) are barely affected by Ni addition. Notably, only very small amounts of methane were formed on NiO(x)−In_2O_3 (x = 1 and 6), which is unusual for Ni-based catalysts. Methanation of CO_2 on Ni is a structure-sensitive reaction,[61] and we infer that the suppression of CH_4 formation on NiO(x)−In_2O_3 (x = 1 and 6) catalysts might be due to the absence of step-edge Ni sites because of the high dispersion of Ni in the reduced catalysts (see below). The following trends were observed when the NiO loading was increased beyond 6 wt %: (i) CO_2 conversion decreased as compared to NiO(6)−In_2O_3 and (ii) CO and CH_4 selectivity increased at the expense of CH_3OH selectivity. Based on these observations and the XRD results, it becomes clear that the In_2O_3 phase plays a pivotal role in the selective CH_3OH synthesis from CO_2, in agreement with earlier reports.[29,30,32] The formation of CH_4 at high NiO loading (x = 75 and 100) can be explained by the formation of metallic Ni particles, which are known to catalyze CO_2 methanation.[61] Figure 4b further shows that the CH_3OH formation rate first increased and then decreased with respect to NiO loading, pointing to a clear Ni−In synergy in CO_2 hydrogenation to CH_3OH. At the optimum NiO loading (6 wt %), the CH_3OH rate is nearly 4 times higher than that of the unpromoted In_2O_3. The time-on-stream (TOS) catalytic performances of In_2O_3, NiO(1)-In_2O_3, and NiO(6)-In_2O_3 are presented in Figure 4c,d, showing that CO_2 conversion and CH_3OH selectivity were stable during the whole test of ~12 h.
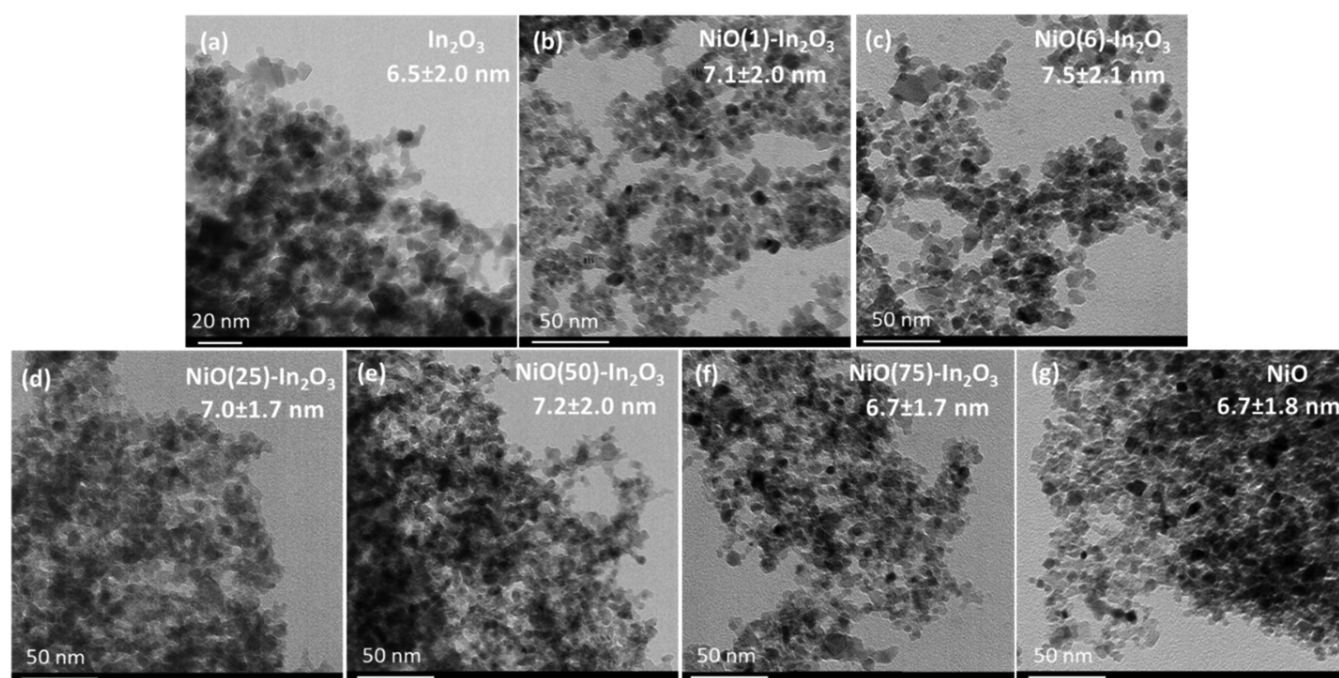
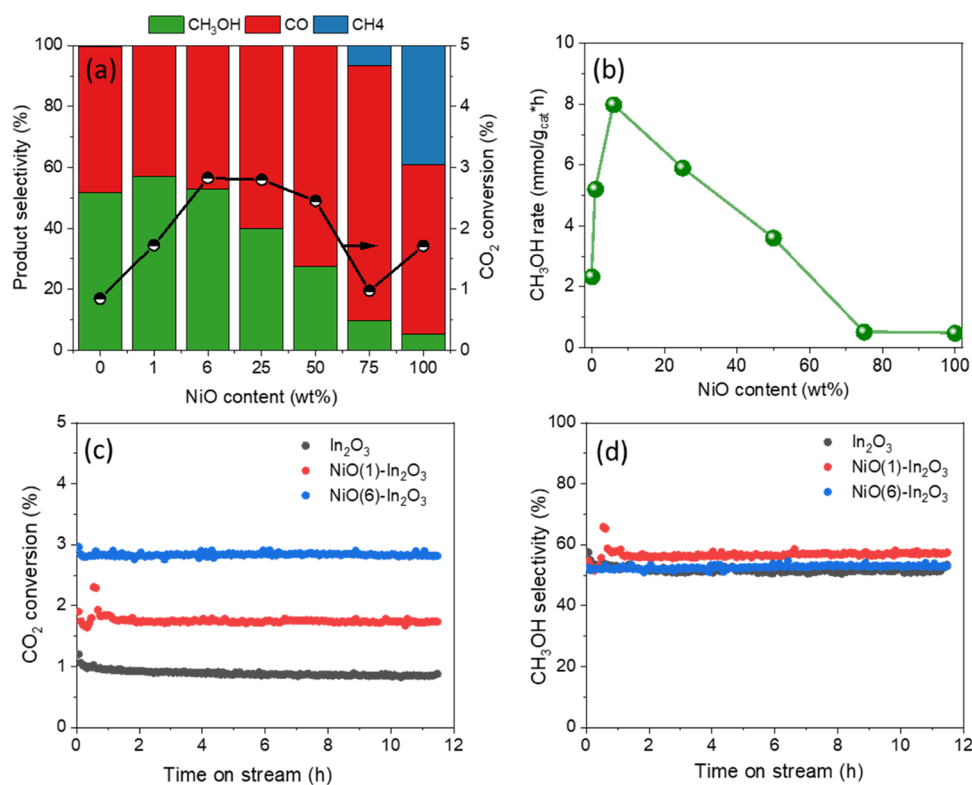**Figure 2.** TEM images of the as-prepared NiO-In$_2$O$_3$ catalysts with varying NiO loadings.

Figure 3. XRD patterns of the as-prepared NiO-In$_2$O$_3$ catalysts with varying NiO loadings.

3.4. Characterization of Ni−In Synergy. N$_2$ physisorption (Table S2) and TEM (Figure S3) measurements were carried out on used In$_2$O$_3$, NiO(1)−In$_2$O$_3$, and NiO(6)−In$_2$O$_3$ catalysts. In comparison with the as-prepared catalysts, the average particle size of the used catalysts is the same after the reaction. This observation demonstrates that the difference in catalyst surface area cannot explain the observed Ni−In synergy.

EPR spectroscopy can be used to study defects and states with unpaired electrons in nickel oxides.[62] The ex situ EPR spectra of the as-prepared samples measured at −173 °C are shown in Figure 5. The NiO bulk reference sample (NiO-ref) does not show an EPR signal. The antiferromagnetic state of bulk stoichiometric NiO can be explained by the very low contribution of disordered surface states. The NiO sample prepared by FSP shows a strong anisotropic EPR signal, which is due to the much smaller crystallite size (ca. 6.7 nm according

to TEM). The ferromagnetic nature of NiO crystals with a size smaller than 10 nm has been described.[63] The NiO(x)-In$_2$O$_3$ ($x \geq 25$) samples show similar broad anisotropic ferromagnetic signals as the FSP-prepared NiO sample, however with different line shapes and intensities. This suggests that these materials contain also small NiO nanoparticles having different sizes and shapes with different anisotropic contributions. The decreasing EPR signal can be attributed to the dilution of NiO with In$_2$O$_3$. The two samples with low NiO loadings, i.e., NiO(1)-In$_2$O$_3$ and NiO(6)-In$_2$O$_3$, show only very weak signals. This implies that Ni is present in a different configuration than in small NiO particles. As it is unlikely that Ni is present as NiO particles at such low NiO loading, we speculate that Ni is present as atomically dispersed 3+ ions in In$_2$O$_3$ or at the In$_2$O$_3$ surface. This was supported by the appearance of a very weak signal (Figure S4), which might be attributed to the presence of isolated Ni^{3+} ions in NiO(1)-In$_2$O$_3$.[64] The presence of Ni^{3+} ions was also suggested by the XPS and XAS results (see below).

Figure 6 shows Ni 2p$_{3/2}$ and In 3d$_{5/2}$ XP spectra of the as-prepared NiO-In$_2$O$_3$ catalysts. Interpretation of the 2p core level of transition-metal oxides with unfilled d-orbitals is complex because of the main line multiplet contributions as well as satellite peaks.[65] The Ni 2p$_{3/2}$ spectrum of the as-prepared NiO is similar to that of polycrystalline NiO with the main lines at binding energies (BEs) of 853.0 and 854.9 eV and a main shake-up feature at 860.1 eV. The spectrum of NiO(75)-In$_2$O$_3$ contains similar lines as NiO, although the contribution around 854.9 eV is less intense. Reducing the NiO loading ($x \leq 50$) leads to a strong decrease of the intensity of the peak at 853.0 eV, indicating the disappearance of NiO particles in these samples. The main peaks at ca. 855.1 eV of NiO(1)-In$_2$O$_3$ and NiO(6)-In$_2$O$_3$ can have different origins. This feature has been linked to Ni^{3+},[66,67] but this assignment is not unequivocal. Similar XP spectra with a main contribution at 855.5 eV (note that BE of C 1s set at 285.0 eV) were also reported for Ni/TiO$_2$ and Ni/CeO$_2$ samples and

Figure 4. (a) CO_2 conversion and product distribution, and (b) CH_3OH rate versus NiO loading. TOS behavior of (c) CO_2 conversion and (d) CH_3OH selectivity over In_2O_3, $NiO(1)-In_2O_3$, and $NiO(6)-In_2O_3$. Conditions: 50 mg of catalyst, 250 °C, 30 bar, and $CO_2:H_2:N_2 = 10:30:10$ mL/min.
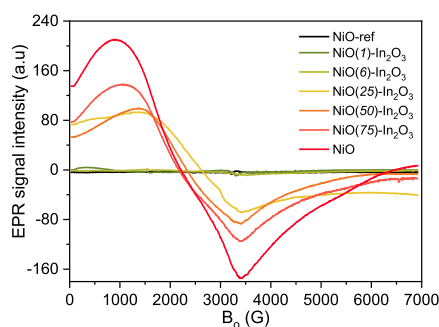

Figure 5. Ex situ EPR spectra (measured at −173 °C) of the as-prepared $NiO-In_2O_3$ catalysts with varying NiO loadings.

could be explained by the presence of very small NiO patches stabilized by strong interactions with the oxide supports.[67] The XP spectra of the In 3d region of $NiO(1)-In_2O_3$ and $NiO(6)-In_2O_3$ show a significant shift of the In $3d_{5/2}$ core line to lower BE in comparison to the spectrum of In_2O_3, which can be associated with Ni substitution in the In_2O_3 lattice.[68] Such a shift is absent in the $NiO(x)-In_2O_3$ ($x \geq 25$) samples, suggesting an electronic structure similar to the In_2O_3 sample.
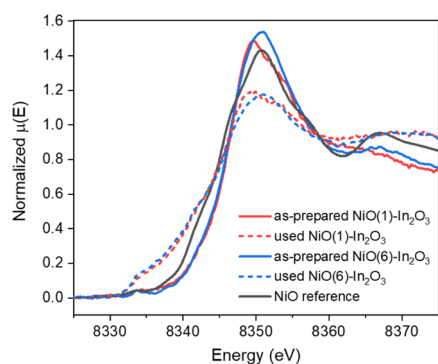
Normalized XANES spectra at the Ni K-edge are presented in Figure 7. The half-edge energies for $NiO(1)-In_2O_3$ and $NiO(6)-In_2O_3$ are, respectively, located at 8344.2 and 8343.9 eV. These values are substantially higher than the half-edge energy of 8342.5 eV observed for NiO, indicating that Ni is in the 3+ state. EXAFS analysis was also used to investigate Ni−In interactions in these two samples. Figure 8a shows that $NiO(1)-In_2O_3$ and $NiO(6)-In_2O_3$ samples contain a Ni−In shell due to the Ni−O−In path.[69] The fit results of the Ni K-

edge EXAFS data (Table 2) show that the CN of the Ni−In (oxidic) shells are 6.3 and 5.3 for the samples with 1 and 6 wt % NiO, respectively. The lower CN of the Ni−In (oxidic) shell for $NiO(6)-In_2O_3$ goes together with the appearance of a Ni-Ni (oxidic) shell (CN = 7.5) due to the Ni−O−Ni path in NiO. The coordination environment of In atoms does not change profoundly among the as-prepared In_2O_3, $NiO(1)-In_2O_3$, and $NiO(6)-In_2O_3$ samples (Figure 8b), which is to be expected due to the high In_2O_3 content in these samples. The fit results of the In K-edge EXAFS data (Table S3) also confirm that the bulk of In_2O_3 does not change significantly after adding small amounts of NiO ($x \leq 6$).

The Ni species in the $NiO(x)-In_2O_3$ ($x = 1$ and 6) samples were also studied by H_2-TPR (Figure 9a). The profile of $NiO(1)-In_2O_3$ contains a single reduction feature at ~300 °C. This feature can be attributed to the reduction of Ni cations substituted in the In_2O_3 lattice. The H_2/Ni ratio corresponding to this feature is ~0.7, indicating that likely only a part of substituted Ni can be reduced. This may be explained by the fact that a part of Ni cations resides in the bulk of In_2O_3. The profile of $NiO(6)-In_2O_3$ contains more reduction features than $NiO(1)-In_2O_3$ after 300 °C. This observation points to the more heterogeneous speciation of Ni in the former sample, which is in line with the earlier EXAFS analysis. Oxygen vacancy (O_v) formation in In_2O_3 was also studied by H_2-TPR measurements. The O_v formation in the as-prepared In_2O_3 sample is characterized by a reduction peak around 200 °C.[39] For the $NiO(1)-In_2O_3$ and $NiO(6)-In_2O_3$ samples, we observed that this reduction feature is broadened compared to In_2O_3, with two distinct peaks being resolved for $NiO(1)-In_2O_3$. These differences can be due to Ni substitution in the In_2O_3 lattice, resulting in a more heterogeneous reduction
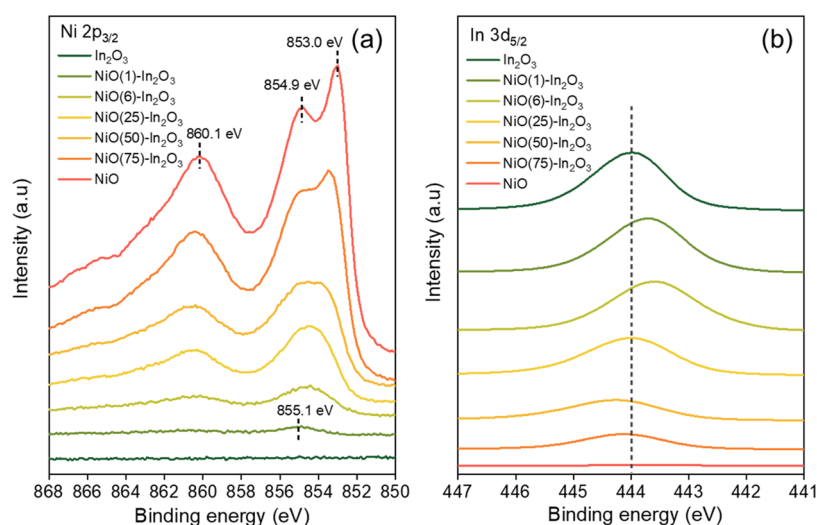
**Figure 6.** Ni $2p_{3/2}$ and In $3d_{5/2}$ XP spectra of the as-prepared NiO-In$_2$O$_3$ catalysts.

Figure 7. Normalized XANES spectra at the Ni K-edge of the as-prepared and used NiO(x)-In$_2$O$_3$ (x = 1 and 6) catalysts with a NiO reference.

behavior of the In$_2$O$_3$ surface. Quantification of these reduction peaks indicates that the O$_v$ densities are 54 and 52 μmol/g$_{cat}$ for NiO(1)-In$_2$O$_3$ and NiO(6)-In$_2$O$_3$, respectively. These values are slightly higher than the value of 42 μmol/g$_{cat}$ for In$_2$O$_3$. The corresponding surface-area-normalized O$_v$ densities are 0.34, 0.49, and 0.53 μmol/m^2 for In$_2$O$_3$, NiO(1)-In$_2$O$_3$, and NiO(6)-In$_2$O$_3$, respectively. Although one may expect a lower O$_v$ density upon Ni substitution because of the stronger Ni−O bond (396 kJ/mol) than the

In−O bond (346 kJ/mol),[68] the presence of smaller Ni cations in In$_2$O$_3$ may distort the In$_2$O$_3$ lattice and weaken the In−O bonds. We also studied the In$_2$O$_3$ surface O$_v$ density from the O 1s XP spectra of the used catalysts (Figure 9b). The peaks at BE of 529.3 and 531.2 eV can be related to lattice O in In$_2$O$_3$ (O$_{lattice}$) and O close to oxygen vacancies (O$_{vacancy}$), respectively.[40] Peak deconvolution indicates that addition of Ni leads to a slight increase of surface O$_v$ density, in agreement with the H$_2$-TPR analysis.

We next compare the Ni $2p_{3/2}$ XP spectra and Ni K-edge XAS data of the as-prepared and used NiO(1)-In$_2$O$_3$ and NiO(6)-In$_2$O$_3$ catalysts to gain insights into the evolution of Ni species under CO$_2$ hydrogenation conditions. Ni reduction is obvious as appreciated from the strong decrease of the Ni component at 855.1 eV and the appearance of a reduced Ni component at 851.9 eV (Figure 10a). Although a large part of Ni is reduced after CO$_2$ hydrogenation, some Ni cations remain in the used catalysts. The Ni reduction also follows from the decrease of the half-edge energies from ∼8344.0 to ∼8341.5 eV in these two samples as shown in Figure 7. The Ni k-edge EXAFS data (Figure 10b and Table 2) show that the Ni−O, Ni−O−Ni, and Ni−O−In contributions strongly decrease after CO$_2$ hydrogenation reactions. For the NiO(1)-In$_2$O$_3$ sample, a strong decrease in the Ni−O and Ni−In (oxidic) shells with final CNs of 1.7 and 2.3 goes
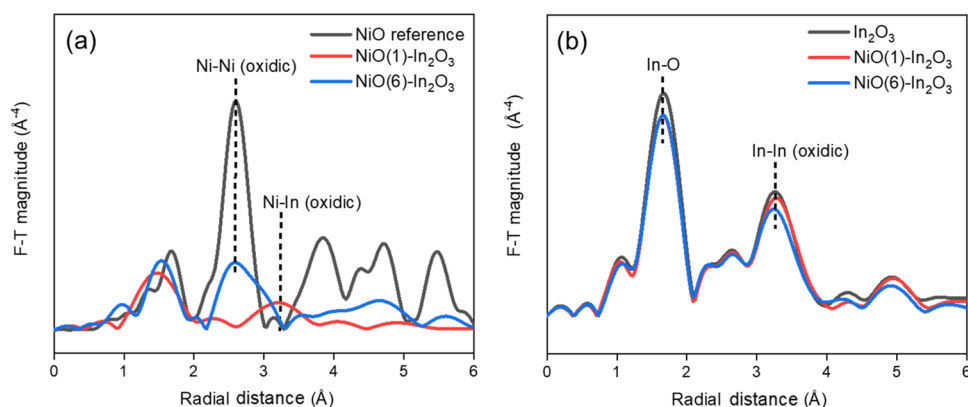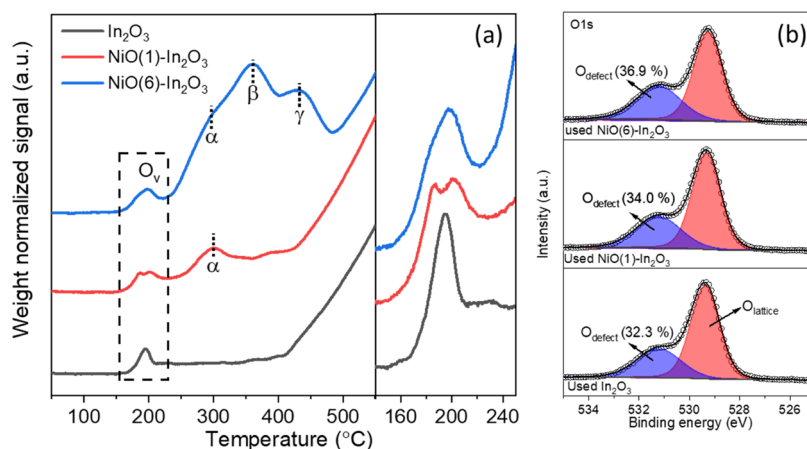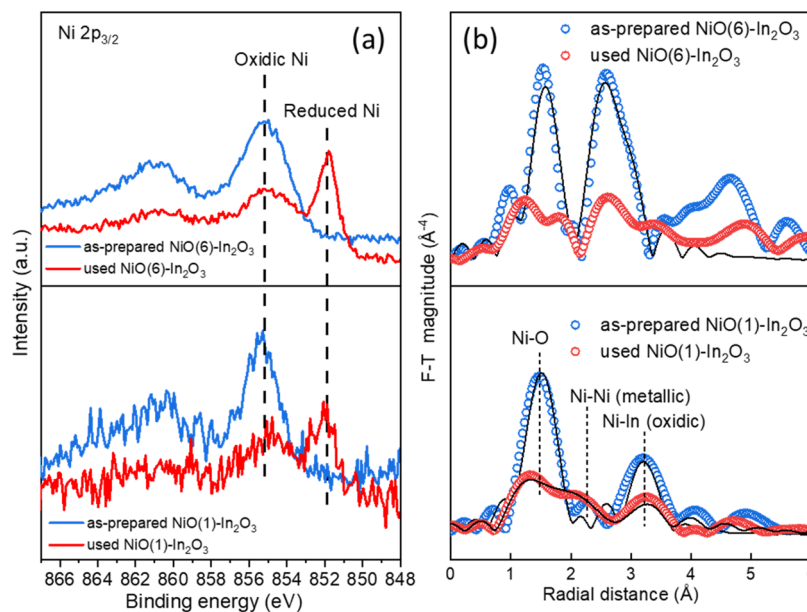

Figure 8. (a) Ni K-edge and (b) In K-edge k^3-weighted R-space plots of the as-prepared (In$_2$O$_3$), NiO(1)-In$_2$O$_3$ and NiO(6)-In$_2$O$_3$ catalysts.

**Table 2. Fit Parameters of the k^3-Weighted EXAFS Spectra at the Ni K-Edge**

	path	r(Å) [±]	CN [±]	δ^2 (Å^2) [±]	r^2
as-prepared NiO(1)-In$_2$O$_3$	Ni–O	2.04 [0.02]	6.0 [1.2]	0.007 [0.004]	0.054
	Ni–In (oxidic)	3.34 [0.05]	6.3 [2.2]	0.016 [0.008]	
used NiO(1)-In$_2$O$_3$	Ni–O	1.97 [0.06]	1.7 [set]	0.001 [0.003]	0.017
	Ni–Ni (metallic)	2.37 [0.06]	7.4 [4.0]	0.032 [0.010]	
	Ni–In (oxidic)	3.33 [0.05]	2.3 [set]	0.007 [0.005]	
as-prepared NiO(6)-In$_2$O$_3$	Ni–O	2.09 [0.03]	6.4 [1.9]	0.007 [0.006]	0.030
	Ni–Ni (oxidic)	3.01 [0.03]	7.5 [5.2]	0.008 [0.007]	
	Ni–In (oxidic)	3.33 [0.28]	5.3 [set]	0.032 [0.037]	
used NiO(6)-In$_2$O$_3$[a]					

[a]No proper fit can be obtained.

Figure 9. (a) H$_2$-TPR profiles of the as-prepared In$_2$O$_3$, NiO(1)-In$_2$O$_3$, and NiO(6)-In$_2$O$_3$ catalysts. (b) O 1s XP spectra of the used In$_2$O$_3$, NiO(1)-In$_2$O$_3$, and NiO(6)-In$_2$O$_3$ catalysts.

Figure 10. (a) Ni 2p$_{3/2}$ XP spectra and (b) Ni K-edge k^3-weighted R-space plots of the as-prepared and used NiO(x)-In$_2$O$_3$ (x = 1 and 6) catalysts.

together with the appearance of a Ni-Ni shell with a CN of 7.4. These observations suggest that a substantial fraction of Ni cations in the as-prepared NiO(6)-In$_2$O$_3$ ($x \leq 6$) samples were reduced into Ni single atoms (SAs) and/or Ni clusters under the reducing reaction conditions.

Finally, in situ EPR spectra confirmed the presence of reduced Ni species and O$_v$ in In$_2$O$_3$ during CO$_2$ hydrogenation

at 250 °C (Figure 11). The weak EPR signal at g = 2.007 in NiO(1)-In$_2$O$_3$ and NiO(6)-In$_2$O$_3$ can be assigned to electrons trapped in anion vacancies of reducible oxides.[70,71] The NiO(6)-In$_2$O$_3$ sample also showed a broad signal at g = 2.273. We attribute this to small ferromagnetic Ni clusters[72] rather than paramagnetic Ni^{3+} since this signal disappeared at −153 °C (Figure S6), most probably due to reoxidation by trace
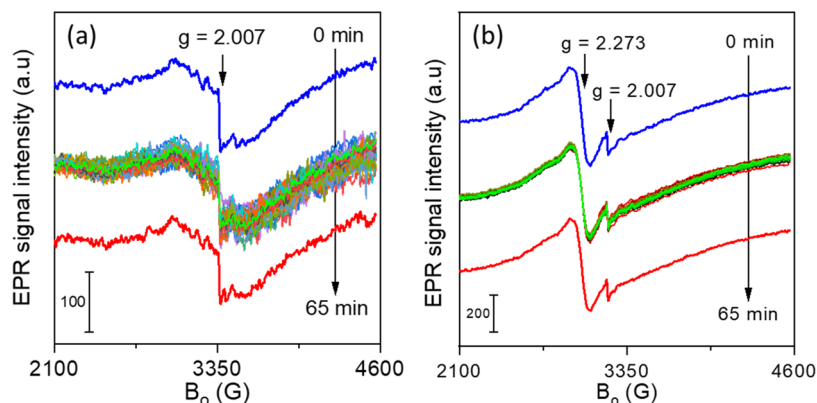
Figure 11. In situ EPR spectra of (a) $NiO(1)$-In_2O_3 and (b) $NiO(6)$-In_2O_3 during CO_2 hydrogenation reaction at 250 °C (1 bar and H_2/CO_2 = 3).
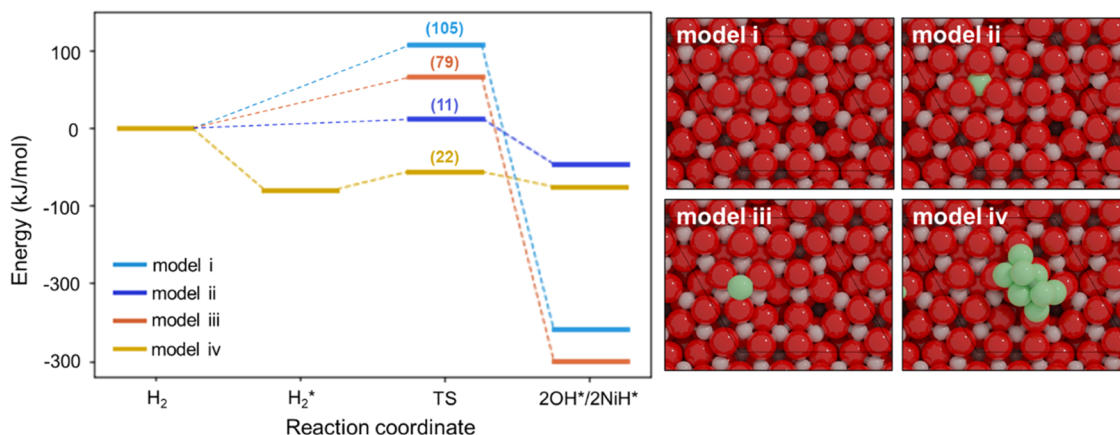
**Figure 12.** Potential energy diagrams for H_2 activation on different (Ni)-In_2O_3 catalyst models with the forward barrier (kJ/mol) of H_2 activation (left) and calculated (Ni)-In_2O_3 catalyst models (right). (O atoms in red, In atoms in brown, and Ni atoms in green).

oxygen or water during purging. Figure S6 also shows that both $NiO(1)$-In_2O_3 and $NiO(6)$-In_2O_3 samples after CO_2 hydrogenation contain a signal at $g = 2.005$ due to the presence of O_v. Notably, the EPR spectra recorded at −153 °C for the catalysts after CO_2 hydrogenation are similar to those after subsequent H_2 reduction at 300 °C.

3.5. Discussion. Based on the EPR, XPS, XAS, and H_2-TPR results, we found that $NiO(1)$-In_2O_3 contains highly dispersed and possibly isolated Ni cations, which mostly substitute for In in the In_2O_3 lattice. The $NiO(6)$-In_2O_3 sample contains additional small Ni-oxide patches stabilized by the In_2O_3 support. Although XPS and XANES provide indications for the presence of Ni^{3+} in these two samples, this is only confirmed for $NiO(1)$-In_2O_3 by EPR, probably due to the strong spin exchange between Ni^{3+} centers at higher Ni loading.[73] Moreover, the H_2-TPR and O 1s XPS results indicate that introduction of Ni cations in the In_2O_3 lattice leads to a higher surface O_v density in comparison to In_2O_3. As oxygen vacancies in In_2O_3 are known to be involved in CO_2 hydrogenation to CH_3OH,[29,30,32] the higher O_v density due to Ni addition can contribute to the improved CH_3OH rate. Nevertheless, we also found that the increase in the CH_3OH rate is much larger (In_2O_3:$NiO(1)$-In_2O_3:$NiO(6)$-$In_2O_3 \approx$ 1:2:4) than the increase in the estimated weight-based O_v density from H_2-TPR (In_2O_3:$NiO(1)$-In_2O_3:$NiO(6)$-$In_2O_3 \approx$ 1:1.3:1.2). This observation suggests that the change in surface O_v density due to Ni addition is not the major reason for the

observed Ni−In synergy. H_2 activation is another important aspect of CO_2 hydrogenation over In_2O_3-based catalysts. It has been demonstrated that heterolytic H_2 dissociation on unpromoted In_2O_3 requires overcoming a high activation barrier of 0.95 eV (∼91 kJ/mol).[32] Slow H_2 dissociation is also in line with the strong dependence of the CH_3OH formation rate on the H_2 partial pressure.[32,43,74] Our characterization of the used $NiO(x)$-In_2O_3 catalysts ($x \leq 6$) demonstrates that a part of oxidic Ni species in the as-prepared catalysts, present as Ni cations substituted in the In_2O_3 lattice and Ni-oxide patches on the In_2O_3 surface, will be in situ-reduced during the CO_2 hydrogenation reaction.

We carried out DFT calculations to determine the influence of difference Ni species on the activation of H_2. Four different model systems were considered, corresponding to (i) the stoichiometric $In_2O_3(111)$ surface, (ii) a Ni single atom doped in the $In_2O_3(111)$ surface, (iii) a Ni single atom located on the $In_2O_3(111)$ surface, and (iv) a Ni_8 cluster on the $In_2O_3(111)$. The potential energy diagrams corresponding to H_2 activation for these models are shown in Figure 12. For the stoichiometric In_2O_3 surface and the substituted Ni atom, H_2 dissociation results in two OH groups, indicative of homolytic dissociation. The reaction over the stoichiometric surface is activated by 105 kJ/mol with an energy of $\Delta E_{ads} = -250$ kJ/mol. These values are in line with an earlier DFT study of H_2 dissociation on the (111) surface of In_2O_3.[43] Doping of a Ni single atom in this surface results in a small decrease of the
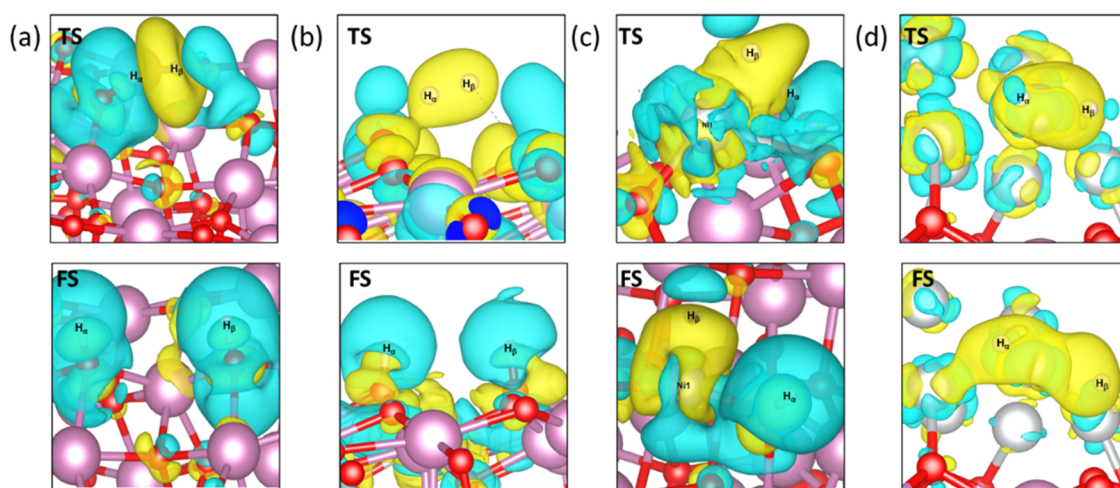
Figure 13. Bader charge analysis of H_2 activation at (a) bare In_2O_3, (b) Ni SA doped In_2O_3, (c) Ni SA on In_2O_3, and (d) Ni_8 cluster on In_2O_3. Yellow and blue surfaces indicate areas of electron accumulation and electron depletion, respectively (iso-value of 0.02 e/Å^3). The charge density difference was calculated by $\Delta\rho = \rho1 - \rho2 - \rho3$ (where $\rho1$, $\rho2$, and $\rho3$ represent the charge densities of the whole system, the support, and the adsorbate, respectively).

activation barrier to 79 kJ/mol. The lower barrier goes together with a more exothermic reaction energy ($\Delta E_{ads} = -300$ kJ/mol) for model ii. For model iii, H_2 activation involves the single Ni atom adsorbed on top of the $In_2O_3(111)$ surface. One of the H atoms remains at the Ni atom, while the other migrates to a neighboring O atom, resulting in, respectively, Ni−H and OH fragments. The barrier associated with H_2 dissociation on this model is only 11 kJ/mol. Similar results have been reported by Frei et al. for a single-atom Ni_1-In_2O_3 model catalyst.[50] H_2 activation over the supported Ni_8 cluster of model iv proceeds in two steps. After adsorption of molecular H_2 with $\Delta E_{ads} = -90$ kJ/mol, H−H bond scission results in two H atoms adsorbed in a bridged configuration. With respect to the gas phase, the process of H_2 activation is barrierless. This elementary reaction step is exothermic by 5 kJ/mol. Dissociative adsorption of H_2 on extended Ni surfaces has been well investigated. Yang et al. reported barrierless activation of H_2 on Ni(111) with an overall exothermicity of 92 kJ/mol.[75] Similar results were reported for different Ni surface terminations as well.[76] Thus, the results for the In_2O_3-supported Ni_8 cluster are in good agreement with those obtained for metallic Ni surfaces.

To rationalize the influence of difference Ni species on H_2 dissociation, we studied the electron density differences as a function of the reaction coordinate of H_2 dissociation for the different surface models. While the final state (FS) of H_2 dissociation on $In_2O_3(111)$ is indicative of homolytic H_2 dissociation, the electron density difference analysis of the transition state (TS) shows electron depletion around one H atom and electron accumulation around the other one (Figure 13a). This is also reflected in the Bader charges, amounting to +0.45|e| and −0.23|e| for H_α and H_β, respectively. Thus, H_2 dissociation involves heterolytic cleavage of the H−H bond, where the positively charged H atom already starts interacting with a surface O atom of the In_2O_3 surface. The relatively high activation energy can then be explained by considering that the negative charge around the other H atom is not well compensated by the oxygen-terminated surface, giving rise to a strong Coulombic repulsion. The two H atoms in the FS have positive charges of +0.61|e| and +0.63|e|, respectively, as expected for surface OH groups. For the Ni single atom doped

inside the In_2O_3 surface (model ii), the same analysis of the TS (Figure 13b) indicates electron accumulation around both H atoms. Bader charge analysis shows that one of the H atoms is nearly neutral (H_α with −0.01|e|), while the other one (H_β) has a positive charge of +0.22|e|. Although the charge on H_α is lower, the radical character of this fragment still results in Coulombic repulsion with the surface, explaining the relatively high activation energies. The final product of the H_2 dissociation reaction is again that of homolytic dissociation. For the Ni atom adsorbed on the In_2O_3 surface (Figure 13c), H_2 dissociates heterolytically with the two H fragments having opposite charges in the TS (H_α with +0.31|e| and H_β with −0.24|e|). The positively charged H_α interacts with one surface O atom of In_2O_3, while the negatively charged H_β interacts with the Ni atom. The charge of the Ni atom before interaction with H_2 is +0.66|e|, which slightly decreases to +0.59|e| in the TS and +0.56|e| in the FS. The favorable electrostatic interactions for both H atoms with the surface in the TS can explain the much lower activation barrier for H_2 dissociation on model iii. The FS of H_2 dissociation is the product of heterolytic dissociation, with H_α acquiring a positive charge (+0.64|e|), indicative of the formation of an OH group. The H_β atom has a slightly negative charge (−0.02|e|), indicative of the formation of a surface hydride adsorbed on the slightly positively charged Ni atom (+0.56|e|). For model iv (Figure 13d), areas of electron accumulation are observed around the H_α and H_β atoms in both the TS and FS. This is also reflected by the negative charges on both H atoms in the TS (−0.1|e| for H_α and H_β) and the FS (−0.19|e| for H_α and −0.22|e| for H_β). Accordingly, we can conclude that the dissociation mechanism of H_2 is homolytic. Compared with model iii, the Ni_8 cluster stabilizes both H atoms through formation of Ni−H bonds, thus further decreasing the overall H_2 dissociation barrier.

These DFT calculations point at the significantly positive influence of reduced Ni species on H_2 activation due to the stabilization of hydride species. While H_2 dissociation on a single Ni atom adsorbed on the In_2O_3 surface would follow a heterolytic dissociation mechanism resulting in Ni−H and OH species, a Ni_8 cluster would result in classical metal-catalyzed homolytic H_2 dissociation. The barriers for these cases are

much lower than those where the surface is terminated by O anions that cannot stabilize the negatively charged H atom during heterolytic dissociation. While our characterization data suggest that part of the Ni atoms may still be doped in the In_2O_3 surface during CO_2 hydrogenation, their role in H_2 activation appears to be limited. Therefore, we conclude that the observed Ni−In synergy can be mainly linked to in situ-reduced Ni species in the form of single atoms or very small clusters. These reduced Ni species can significantly facilitate the dissociative adsorption of H_2, which otherwise requires a high activation barrier on the unpromoted In_2O_3 surface. A similar mechanism of metal promotion was reported for other metal-promoted In_2O_3 catalysts.[42,43,49,77] For example, a detailed study from Perez-Ramirez's group[43] emphasized the role of finely dispersed Pd clusters in the H_2 activation and the role of H atoms in the following hydrogenation steps of adsorbed CO_2. We also briefly discuss here our results in comparison to those recently reported by Frei et al., who prepared Ni/In_2O_3 catalysts by dry impregnation.[50] In line with our work, Ni promotes CH_3OH formation at low Ni loading, whereas higher Ni loading leads to CO and CH_4 formation. In the work of Frei et al., evidence was found for the formation of an $InNi_3$ phase by synchrotron XRD measurements. Our characterization data, however, do not provide strong evidence for the formation of such an alloy.

We next compare the FSP-prepared $NiO−In_2O_3$ catalysts in this study to other metal-promoted In_2O_3 catalysts. Using the FSP method, well-defined In_2O_3-based catalysts with tunable chemical composition can be prepared. The obtained catalysts have similar surface areas. These aspects render FSP an efficient method to study the influence of promoters on In_2O_3-based catalysts. We also found that metal promoters are better dispersed in In_2O_3 by FSP preparation in comparison with conventional preparation methods. This leads, among others, to Ni substitution in the In_2O_3 lattice, which is less likely to take place during impregnation. The high Ni dispersion in the oxide precursor also leads to a stronger Ni−In synergy in CO_2 hydrogenation to methanol. Specifically, the activity of the optimum $NiO−In_2O_3$ catalyst in this study is about 4 times higher than that of the In_2O_3 reference catalyst, while the synergetic effect is less pronounced in other studies of Ni-promoted In_2O_3 catalysts.[49,50,78] As shown in Table S4, the $NiO(6)−In_2O_3$ catalyst in this study is compared to other Ni-promoted In_2O_3 catalysts with respect to their performance in CO_2 hydrogenation. To make such a comparison, we also performed additional catalytic tests at higher temperatures (275 and 300 °C) using the $NiO(6)−In_2O_3$ catalyst. In comparison to the work by Jia et al., our $NiO−In_2O_3$ catalyst shows a slightly higher methanol rate at 250 °C (0.26 vs 0.21 mmol g_{cat}^{-1} h^{-1}), while the rates at higher temperatures of 275 and 300 °C are a bit lower.[2] In addition, the methanol rate of our $NiO−In_2O_3$ catalyst at 275 °C (0.36 mmol g_{cat}^{-1} h^{-1}) is similar to the rates reported in the literature for other Ni-promoted In_2O_3 catalysts (0.36 mmol g_{cat}^{-1} h^{-1} at 270 °C and 0.34 mmol g_{cat}^{-1} h^{-1} at 280 °C).[3,4] The methanol selectivity of our $NiO−In_2O_3$ catalyst is somewhat lower than the reported values, which can be explained by the lower reaction pressure used in our catalytic tests (30 vs 50 bar in the cited literature).

4. CONCLUSIONS

Aiming at improving the performance of In_2O_3 in the hydrogenation of CO_2 to CH_3OH, a bimetallic Ni−In system was identified as a potential replacement for $Pd−In_2O_3$,

outperforming $Co−In_2O_3$ and $Cu−In_2O_3$. FSP-prepared $NiO−In_2O_3$ catalysts are made up from small (∼7 nm) particles with a high surface area. Strong Ni−In synergy is noted for CH_3OH synthesis from CO_2 with an optimal NiO loading of 6 wt %. In the as-prepared $NiO−In_2O_3$ catalysts, a small amount of Ni is substituted in In_2O_3, with the remainder being present as highly dispersed Ni-oxide for the samples with a low NiO loading (≤6 wt %). At higher NiO loading (≥50 wt %), Ni is mainly present as bulk NiO particles. H_2-TPR points to a higher surface O_v density for the $NiO(x)−In_2O_3$ ($x = 1$ and 6) catalysts in comparison to the unpromoted In_2O_3, indicating that Ni substitution can destabilize the In_2O_3 lattice to some extent. XPS, XAS, and EPR data demonstrate that the use of $NiO(x)−In_2O_3$ ($x = 1$ and 6) catalysts in CO_2 hydrogenation leads to the reduction of Ni cations and the formation of Ni SAs and/or Ni clusters. In addition to a higher surface O_v density relevant to CO_2 adsorption, DFT calculations suggest that the observed Ni−In synergy in CH_3OH synthesis from CO_2 is mainly originated from the formation of reduced Ni species on the In_2O_3 surface, which enhances the rate of H_2 dissociation and following hydrogenation of CO_2 adsorbed on O_v.

■ ASSOCIATED CONTENT

Ⓢ Supporting Information

The Supporting Information is available free of charge at https://pubs.acs.org/doi/10.1021/acscatal.1c03170.

> Additional characterization (XRD and H_2-TPR) and catalytic results of the $M−In_2O_3$ catalysts (Figures S1 and S2 and Table S1); N_2 physisorption and TEM results of the used $NiO−In_2O_3$ catalysts (Figure S3 and Table S2); zoom-in of the ex situ EPR spectrum of $NiO(1)−In_2O_3$ (Figure S4); EXAFS data at the In K-edge with corresponding fit parameters (Figure S5 and Table S3); EPR spectra recorded after CO_2 hydrogenation and subsequent H_2 reduction (Figure S6); and comparison of CO_2 hydrogenation performance over different indium-based catalysts (Table S4) (PDF)

■ AUTHOR INFORMATION

Corresponding Author

Emiel J. M. Hensen − *Laboratory of Inorganic Materials and Catalysis, Department of Chemical Engineering and Chemistry, Eindhoven University of Technology, 5600 MB Eindhoven, The Netherlands;* ⓘ orcid.org/0000-0002-9754-2417; Email: e.j.m.hensen@tue.nl

Authors

Jiadong Zhu − *Laboratory of Inorganic Materials and Catalysis, Department of Chemical Engineering and Chemistry, Eindhoven University of Technology, 5600 MB Eindhoven, The Netherlands*

Francesco Cannizzaro − *Laboratory of Inorganic Materials and Catalysis, Department of Chemical Engineering and Chemistry, Eindhoven University of Technology, 5600 MB Eindhoven, The Netherlands*

Liang Liu − *Laboratory of Inorganic Materials and Catalysis, Department of Chemical Engineering and Chemistry, Eindhoven University of Technology, 5600 MB Eindhoven, The Netherlands*

Hao Zhang − *Laboratory of Inorganic Materials and Catalysis, Department of Chemical Engineering and*

Chemistry, Eindhoven University of Technology, 5600 MB Eindhoven, The Netherlands

Nikolay Kosinov − *Laboratory of Inorganic Materials and Catalysis, Department of Chemical Engineering and Chemistry, Eindhoven University of Technology, 5600 MB Eindhoven, The Netherlands;* orcid.org/0000-0001-8520-4886

Ivo. A. W. Filot − *Laboratory of Inorganic Materials and Catalysis, Department of Chemical Engineering and Chemistry, Eindhoven University of Technology, 5600 MB Eindhoven, The Netherlands;* orcid.org/0000-0003-1403-8379

Jabor Rabeah − *Leibniz-Institut für Katalyse an der Universität Rostock e. V., D-18059 Rostock, Germany;* orcid.org/0000-0003-2162-0981

Angelika Brückner − *Leibniz-Institut für Katalyse an der Universität Rostock e. V., D-18059 Rostock, Germany;* orcid.org/0000-0003-4647-1273

Complete contact information is available at:
https://pubs.acs.org/10.1021/acscatal.1c03170

Notes
The authors declare no competing financial interest.

■ REFERENCES

(1) He, M.; Sun, Y.; Han, B. Green Carbon Science: Scientific Basis for Integrating Carbon Resource Processing, Utilization, and Recycling. *Angew. Chem., Int. Ed.* **2013**, *52*, 9620−9633.

(2) Centi, G.; Quadrelli, E. A.; Perathoner, S. Catalysis for CO2 Conversion: A Key Technology for Rapid Introduction of Renewable Energy in the Value Chain of Chemical Industries. *Energy Environ. Sci.* **2013**, *6*, 1711−1731.

(3) Rogelj, J.; Den Elzen, M.; Höhne, N.; Fransen, T.; Fekete, H.; Winkler, H.; Schaeffer, R.; Sha, F.; Riahi, K.; Meinshausen, M. Paris Agreement Climate Proposals Need a Boost to Keep Warming Well below 2 °c. *Nature* **2016**, *534*, 631−639.

(4) Jiang, X.; Nie, X.; Guo, X.; Song, C.; Chen, J. G. Recent Advances in Carbon Dioxide Hydrogenation to Methanol via Heterogeneous Catalysis. *Chem. Rev.* **2020**, *120*, 7984−8034.

(5) Zhong, J.; Yang, X.; Wu, Z.; Liang, B.; Huang, Y.; Zhang, T. State of the Art and Perspectives in Heterogeneous Catalysis of CO2 Hydrogenation to Methanol. *Chem. Soc. Rev.* **2020**, *49*, 1385−1413.

(6) Yang, H.; Zhang, C.; Gao, P.; Wang, H.; Li, X.; Zhong, L.; Wei, W.; Sun, Y. A Review of Catalytic Hydrogenation of Carbon Dioxide into Value-Added Hydrocarbons. *Catal. Sci. Technol.* **2017**, *7*, 4580−4598.

(7) Álvarez, A.; Bansode, A.; Urakawa, A.; Bavykina, A. V.; Wezendonk, T. A.; Makkee, M.; Gascon, J.; Kapteijn, F. Challenges in the Greener Production of Formates/Formic Acid, Methanol, and DME by Heterogeneously Catalyzed CO2 Hydrogenation Processes. *Chem. Rev.* **2017**, *117*, 9804−9838.

(8) Gumber, S.; Gurumoorthy, A. V. P. Methanol Economy Versus Hydrogen Economy. In *Methanol: Science and Engineering*; Elsevier B.V., 2018; pp 661−674.

(9) Olah, G. A. Beyond Oil and Gas: The Methanol Economy. *Angew. Chem., Int. Ed.* **2005**, *44*, 2636−2639.

(10) Goeppert, A.; Czaun, M.; Jones, J.-P.; Surya Prakash, G. K.; Olah, G. A. Recycling of Carbon Dioxide to Methanol and Derived Products − Closing the Loop. *Chem. Soc. Rev.* **2014**, *43*, 7995−8048.

(11) Behrens, M.; Studt, F.; Kasatkin, I.; Kühl, S.; Hävecker, M.; Abild-pedersen, F.; Zander, S.; Girgsdies, F.; Kurr, P.; Kniep, B.; Tovar, M.; Fischer, R. W.; Nørskov, J. K.; Schlögl, R. The Active Site of Methanol Synthesis over Cu/ZnO/Al2O3 Industrial Catalysts. *Science* **2012**, *336*, 893−897.

(12) Sehested, J. Industrial and Scientific Directions of Methanol Catalyst Development. *J. Catal.* **2019**, *371*, 368−375.

(13) Behrens, M. Promoting the Synthesis of Methanol: Understanding the Requirements for an Industrial Catalyst for the Conversion of CO2. *Angew. Chem., Int. Ed.* **2016**, *55*, 14906−14908.

(14) Liang, B.; Ma, J.; Su, X.; Yang, C.; Duan, H.; Zhou, H.; Deng, S.; Li, L.; Huang, Y. Investigation on Deactivation of Cu/ZnO/Al2O3 Catalyst for CO2 Hydrogenation to Methanol. *Ind. Eng. Chem. Res.* **2019**, *58*, 9030−9037.

(15) Prašnikar, A.; Pavlišič, A.; Ruiz-Zepeda, F.; Kovač, J.; Likozar, B. Mechanisms of Copper-Based Catalyst Deactivation during CO2 Reduction to Methanol. *Ind. Eng. Chem. Res.* **2019**, *58*, 13021−13029.

(16) Wu, J.; Masami, T.; Taiki, W.; M, S. The Stability of Cu/ZnO-Based Catalysts in Methanol Synthesis from a CO2-Rich Feed and from a CO-Rich Feed. *Appl. Catal., A* **2001**, *218*, 235−240.

(17) Yang, B.; Li, L.; Jia, Z.; Liu, X.; Zhang, C.; Guo, L. Comparative Study of CO2 Hydrogenation to Methanol on Cubic Bixbyite-Type and Rhombohedral Corundum-Type Indium Oxide. *Chin. Chem. Lett.* **2020**, *31*, 2627−2633.

(18) Li, K.; Chen, J. G. CO2 Hydrogenation to Methanol over ZrO2-Containing Catalysts: Insights into ZrO2 Induced Synergy. *ACS Catal.* **2019**, *9*, 7840−7861.

(19) Wang, Y. H.; Gao, W. G.; Wang, H.; Zheng, Y. E.; Na, W.; Li, K. Z. Structure−Activity Relationships of Cu−ZrO2 Catalysts for CO2 Hydrogenation to Methanol: Interaction Effects and Reaction Mechanism. *RSC Adv.* **2017**, *7*, 8709−8717.

(20) Larmier, K.; Liao, W.-C.; Tada, S.; Lam, E.; Verel, R.; Bansode, A.; Urakawa, A.; Comas-Vives, A.; Copéret, C. CO2 -to-Methanol Hydrogenation on Zirconia-Supported Copper Nanoparticles: Reaction Intermediates and the Role of the Metal-Support Interface. *Angew. Chem., Int. Ed.* **2017**, *56*, 2318−2323.

(21) Ro, I.; Liu, Y.; Ball, M. R.; Jackson, D. H. K.; Chada, J. P.; Sener, C.; Kuech, T. F.; Madon, R. J.; Huber, G. W.; Dumesic, J. A. Role of the Cu-ZrO2 Interfacial Sites for Conversion of Ethanol to Ethyl Acetate and Synthesis of Methanol from CO 2 and H 2. *ACS Catal.* **2016**, *6*, 7040−7050.

(22) Wang, J.; Li, G.; Li, Z.; Tang, C.; Feng, Z.; An, H.; Liu, H.; Liu, T.; Li, C. A Highly Selective and Stable ZnO-ZrO2 Solid Solution Catalyst for CO2 Hydrogenation to Methanol. *Sci. Adv.* **2017**, *3*, No. e1701290.

(23) Li, C.-S.; Melaet, G.; Ralston, W. T.; An, K.; Brooks, C.; Ye, Y.; Liu, Y.-S. S.; Zhu, J.; Guo, J.; Alayoglu, S.; Somorjai, G. A. High-Performance Hybrid Oxide Catalyst of Manganese and Cobalt for Low-Pressure Methanol Synthesis. *Nat. Commun.* **2015**, *6*, 6538−6542.

(24) Posada-Pérez, S.; Vines, F.; Ramirez, P. J.; Vidal, A. B.; Rodriguez, J. A.; Illas, F. The Bending Machine: CO2 Activation and Hydrogenation on Delta-MoC(001) and Beta-Mo2C(001) Surfaces. *Phys. Chem. Chem. Phys.* **2014**, *16*, 14912−14921.

(25) Kunkel, C.; Vines, F.; Illas, F. Transition Metal Carbides as Novel Materials for CO2 Capture, Storage, and Activation. *Energy Environ. Sci.* **2016**, *9*, 141−144.

(26) Duyar, M. S.; Tsai, C.; Snider, J. L.; Singh, J. A.; Gallo, A.; Yoo, J. S.; Medford, A. J.; Abild-Pedersen, F.; Studt, F.; Kibsgaard, J.; Bent, S. F.; Nørskov, J. K.; Jaramillo, T. F. A Highly Active Molybdenum Phosphide Catalyst for Methanol Synthesis from CO and CO2. *Angew. Chem., Int. Ed.* **2018**, *57*, 15045−15050.

(27) Sharafutdinov, I.; Elkjær, C. F.; Pereira de Carvalho, H. W.; Gardini, D.; Chiarello, G. L.; Damsgaard, C. D.; Wagner, J. B.; Grunwaldt, J.; Dahl, S.; Chorkendorff, I.; et al. Intermetallic Compounds of Ni and Ga as Catalysts for the Synthesis of Methanol. *J. Catal.* **2014**, *320*, 77−88.

(28) Fiordaliso, E. M.; Sharafutdinov, I.; Carvalho, H. W. P.; Grunwaldt, J. D.; Hansen, T. W.; Chorkendorff, I.; Wagner, J. B.; Damsgaard, C. D. Intermetallic GaPd2 Nanoparticles on SiO2 for Low-Pressure CO2 Hydrogenation to Methanol: Catalytic Performance and in Situ Characterization. *ACS Catal.* **2015**, *5*, 5827−5836.

(29) Ye, J.; Liu, C.; Ge, Q. DFT Study of CO2 Adsorption and Hydrogenation on the In2O3 Surface. *J. Phys. Chem. C* **2012**, *116*, 7817−7825.

(30) Ye, J.; Liu, C.; Mei, D.; Ge, Q. Active Oxygen Vacancy Site for Methanol Synthesis from CO2Hydrogenation on In2O3(110): A DFT Study. *ACS Catal.* **2013**, *3*, 1296−1306.

(31) Sun, K.; Fan, Z.; Ye, J.; Yan, J.; Ge, Q.; Li, Y.; He, W.; Yang, W.; Liu, C. Hydrogenation of CO2 to Methanol over In2O3 Catalyst. *J. CO2 Util.* **2015**, *12*, 1−6.

(32) Frei, M. S.; Capdevila-Cortada, M.; García-Muelas, R.; Mondelli, C.; López, N.; Stewart, J. A.; Curulla Ferré, D.; Pérez-Ramírez, J. Mechanism and Microkinetics of Methanol Synthesis via CO2 Hydrogenation on Indium Oxide. *J. Catal.* **2018**, *361*, 313−321.

(33) Dang, S.; Qin, B.; Yang, Y.; Wang, H.; Cai, J.; Han, Y.; Li, S.; Gao, P.; Sun, Y. Rationally Designed Indium Oxide Catalysts for CO2 Hydrogenation to Methanol with High Activity and Selectivity. *Sci. Adv.* **2020**, *6*, No. eaaz2060.

(34) Frei, M. S.; Mondelli, C.; Cesarini, A.; Krumeich, F.; Hauert, R.; Stewart, J. A.; Ferre, D. C.; Pe, J. Role of Zirconia in Indium Oxide-Catalyzed CO2 Hydrogenation to Methanol. *ACS Catal.* **2020**, *10*, 1133−1145.

(35) Jiang, X.; Wang, Y.; Gu, D.; Chen, C.; Jiang, L.; Takehira, K.; et al. A Combined Experimental and DFT Study of H2O Effect on In2O3/ZrO2 Catalyst for CO2 Hydrogenation to Methanol. *J. Catal.* **2020**, *383*, 283−296.

(36) Chen, T.; Cao, C.; Chen, T.; Ding, X.; Huang, H.; Shen, L.; Cao, X.; Zhu, M.; Xu, J.; Gao, J.; Han, Y.-F. Unraveling Highly Tunable Selectivity in CO2 Hydrogenation over Bimetallic In-Zr Oxide Catalysts. *ACS Catal.* **2019**, *9*, 8785−8797.

(37) Chou, C.-Y.; Lobo, R. F. Direct Conversion of CO2 into Methanol over Promoted Indium-Based Catalysts. *Appl. Catal., A* **2019**, *583*, 117144−117152.

(38) Dou, M.; Zhang, M.; Chen, Y.; Yu, Y. Theoretical Study of Methanol Synthesis from CO2 and CO Hydrogenation on the Surface of ZrO2 Supported In2O3catalyst. *Surf. Sci.* **2018**, *672−673*, 7−12.

(39) Martin, O.; Martin, A. J.; Mondelli, C.; Mitchell, S.; Segawa, T. F.; Hauert, R.; Drouilly, C.; Curulla-Ferre, D.; Perez-Ramirez, J. Indium Oxide as a Superior Catalyst for Methanol Synthesis by CO2 Hydrogenation. *Angew. Chem., Int. Ed.* **2016**, *55*, 6261−6265.

(40) Hong, Z.; Cao, Y.; Deng, J.; Fan, K. CO2 Hydrogenation to Methanol over Pd/In2O3: Effects of Pd and Oxygen Vacancy. *Appl. Catal., B* **2017**, *82*, 2−9.

(41) García-Trenco, A.; Regoutz, A.; White, E. R.; Payne, D. J.; Shaffer, M. S. P.; Williams, C. K. PdIn Intermetallic Nanoparticles for the Hydrogenation of CO2 to Methanol. *Appl. Catal., B* **2018**, *220*, 9−18.

(42) Snider, J. L.; Streibel, V.; Hubert, M. A.; Choksi, T. S.; Valle, E.; Upham, D. C.; Schumann, J.; Duyar, M. S.; Gallo, A.; Abild-Pedersen, F.; Jaramillo, T. F. Revealing the Synergy between Oxide and Alloy Phases on the Performance of Bimetallic In-Pd Catalysts for CO2 Hydrogenation to Methanol. *ACS Catal.* **2019**, *9*, 3399−3412.

(43) Frei, M. S.; Mondelli, C.; García-Muelas, R.; Kley, K. S.; Puértolas, B.; López, N.; Safonova, O. V.; Stewart, J. A.; Curulla Ferré, D.; Pérez-Ramírez, J. Atomic-Scale Engineering of Indium Oxide

Promotion by Palladium for Methanol Production via CO2 Hydrogenation. *Nat. Commun.* **2019**, *10*, 1−11.

(44) Ye, J.; Liu, C. J.; Mei, D.; Ge, Q. Methanol Synthesis from CO2 Hydrogenation over a Pd4/In2O3 Model Catalyst: A Combined DFT and Kinetic Study. *J. Catal.* **2014**, *317*, 44−53.

(45) Bavykina, A.; Yarulina, I.; Al Abdulghani, A. J.; Gevers, L. E.; Hedhili, M. N.; Miao, X.-H.; Ramirez, A.; Pustovarenko, A.; Dikhtiarenko, A.; Cadiau, A.; Aguilar Tapia, A.; Hazemann, J. L.; Kozlov, S. M.; Ould-Chikh, S.; Cavallo, L.; Gascon, J. Turning a Methanation Co Catalyst into an In-Co Methanol Producer. *ACS Catal.* **2019**, *9*, 6910−6918.

(46) Pustovarenko, A.; Dikhtiarenko, A.; Bavykina, A.; Gevers, L. E.; Ramirez, A.; Telalovic, S.; Aguilar, A.; Hazemann, J. L.; Ould-chikh, S.; Gascon, J.; et al. Metal Organic Framework Derived Synthesis of Cobalt Indium Catalysts for the Hydrogenation of CO 2 to Methanol. *ACS Catal.* **2020**, *10*, 5064−5076.

(47) Shi, Z.; Tan, Q.; Tian, C.; Pan, Y.; Sun, X.; Zhang, J.; Wu, D. CO2 Hydrogenation to Methanol over Cu-In Intermetallic Catalysts: Effect of Reduction Temperature. *J. Catal.* **2019**, *379*, 78−89.

(48) Richard, A. R.; Fan, M. Low-Pressure Hydrogenation of CO2 to CH3OH Using Ni-In-Al/SiO2 Catalyst Synthesized via a Phyllosilicate Precursor. *ACS Catal.* **2017**, *7*, 5679−5692.

(49) Jia, X.; Sun, K.; Wang, J.; Shen, C.; Liu, C. j. Selective Hydrogenation of CO2 to Methanol over Ni/In2O3 Catalyst. *J. Energy Chem.* **2020**, *50*, 409−415.

(50) Frei, M. S.; Mondelli, C.; Safonova, O. V.; López, N.; García-muelas, R.; Morales-vidal, J.; Philipp, M.; Stewart, J. A.; Ferré, D. C.; Pérez-ramírez, J. Nanostructure of Nickel-Promoted Indium Oxide Catalysts Drives Selectivity in CO2 Hydrogenation. *Nat. Commun.* **2021**, *12*, No. 1960.

(51) Teoh, W. Y.; Amal, R.; Mädler, L. Flame Spray Pyrolysis: An Enabling Technology for Nanoparticles Design and Fabrication. *Nanoscale* **2010**, *2*, 1324−1347.

(52) Koirala, R.; Pratsinis, S. E.; Baiker, A. Synthesis of Catalytic Materials in Flames: Opportunities and Challenges. *Chem. Soc. Rev.* **2016**, *45*, 3053−3068.

(53) Ravel, B.; Newville, M. ATHENA, ARTEMIS, HEPHAESTUS: Data Analysis for X-Ray Absorption Spectroscopy Using IFEFFIT. *J. Synchrotron Radiat.* **2005**, *12*, 537−541.

(54) Kresse, G.; Hafner, J. Ab Initio Molecular-Dynamics Simulation of the Liquid-Metalamorphous- Semiconductor Transition in Germanium. *Phys. Rev. B* **1994**, *49*, 14251−14269.

(55) Kresse, G.; Furthmüller, J. Efficiency of Ab-Initio Total Energy Calculations for Metals and Semiconductors Using a Plane-Wave Basis Set. *Comput. Mater. Sci.* **1996**, *6*, 15−50.

(56) Henkelman, G.; Jónsson, H. Improved Tangent Estimate in the Nudged Elastic Band Method for Finding Minimum Energy Paths and Saddle Points. *J. Chem. Phys.* **2000**, *113*, 9978−9985.

(57) Heidrich, D.; Quapp, W. Saddle Points of Index 2 on Potential Energy Surfaces and Their Role in Theoretical Reactivity Investigations. *Theor. Chim. Acta* **1986**, *70*, 89−98.

(58) Hondow, N. S.; Chou, Y. H.; Sader, K.; Douthwaite, R. E.; Brydson, R. Electron Microscopy of Cocatalyst Nanostructures on Semiconductor Photocatalysts. *ChemCatChem* **2011**, *3*, 990−998.

(59) Chen, L.; Horiuchi, T.; Mori, T. Catalytic Reduction of NO over a Mechanical Mixture of NiGa2O4 Spinel with Manganese Oxide: Influence of Catalyst Preparation Method. *Appl. Catal., A* **2001**, *209*, 97−105.

(60) Tasaki, J.; Izushi, T.; Ito, T. Preparation and Characterization of a Phase between NiO and In2O3. *Adv. Ceram.* **1985**, *15*, 169−174.

(61) Vogt, C.; Groeneveld, E.; Kamsma, G.; Nachtegaal, M.; Lu, L.; Kiely, C. J.; Berben, P. H.; Meirer, F.; Weckhuysen, B. M. Unravelling Structure Sensitivity in CO2 Hydrogenation over Nickel. *Nat. Catal.* **2018**, *1*, 127−134.

(62) Dyrek, K.; Che, M. EPR as a Tool to Investigate the Transition Metal Chemistry on Oxide Surfaces. *Chem. Rev.* **1997**, *97*, 305−331.

(63) Rubinstein, M.; Kodama, R. H.; Makhlouf, S. A. Electron Spin Resonance Study of NiO Antiferromagnetic Nanoparticles. *J. Magn. Magn. Mater.* **2001**, *234*, 289−293.

(64) Lovecchio, F. V.; Gore, E. S.; Busch, D. H. The Oxidation and Reduction of Macrocyclic Complexes of Nickel. Electrochemical and Electron Spin Resonance Studies. *J. Am. Chem. Soc.* **1974**, *96*, 3109−3118.

(65) Grosvenor, A. P.; Biesinger, M. C.; Smart, R. S. C.; McIntyre, N. S. New Interpretations of XPS Spectra of Nickel Metal and Oxides. *Surf. Sci.* **2006**, *600*, 1771−1779.

(66) Mansour, A. N. Characterization of LiNiO 2 by XPS. *Surf. Sci. Spectra* **1994**, *3*, 279−286.

(67) Davidson, A.; Tempere, J. F.; Che, M.; Roulet, H.; Dufour, G. Spectroscopic Studies of Nickel(II) and Nickel(III) Species Generated upon Thermal Treatments of Nickel/Ceria-Supported Materials. *J. Phys. Chem. A* **1996**, *100*, 4919−4929.

(68) Li, Y.; Xu, W.; Liu, W.; Han, S.; Cao, P.; Fang, M.; Zhu, D.; Lu, Y. High-Performance Thin-Film Transistors with Aqueous Solution-Processed NiInO Channel Layer. *ACS Appl. Electron. Mater.* **2019**, *1*, 1842−1851.

(69) An, Y.; Wang, S.; Feng, D.; Wu, Z.; Liu, J. Correlation between Oxygen Vacancies and Magnetism in Fe-Doped In 2 O 3 Films. *Appl. Surf. Sci.* **2013**, *276*, 535−538.

(70) Claus, P.; Bruckner, A.; Mohr, C.; Hofmeister, H. Supported Gold Nanoparticles from Quantum Dot to Mesoscopic Size Scale: Effect of Electronic and Structural Properties on Catalytic Hydrogenation of Conjugated Functional Groups. *J. Am. Chem. Soc.* **2000**, *122*, 11430−11439.

(71) Guha, P.; Kar, S.; Chaudhuri, S. Direct Synthesis of Single Crystalline In2O3 Nanopyramids and Nanocolumns and Their Photoluminescence Properties. *Appl. Phys. Lett.* **2004**, *85*, 3851−3853.

(72) Altınçekiç, T. G.; Boz, I.; Basaran, A. C.; Aktas, B.; Kazan, S. Synthesis and Characterization of Ferromagnetic Nickel Nanoparticles. *J. Supercond. Novel Magn.* **2012**, *25*, 2771−2775.

(73) Xiao, Y.; Liu, T.; Liu, J.; He, L.; Chen, J.; Zhang, J.; Luo, P.; Lu, H.; Wang, R.; Zhu, W.; et al. Insight into the Origin of Lithium/Nickel Ions Exchange in Layered Li(NixMnyCoz)O2 Cathode Materials. *Nano Energy* **2018**, *49*, 77−85.

(74) Frei, M. S.; Mondelli, C.; Pérez-Ramírez, J. Development of In2O3-Based Catalysts for CO2-Based Methanol Production. *Chimia* **2020**, *74*, 257−262.

(75) Yang, H.; Whitten, J. L. Dissociative Adsorption of H2 on Ni(111). *J. Chem. Phys.* **1993**, *98*, 5039−5049.

(76) Kresse, G. Dissociation and Sticking of H2 on the Ni(111), (100), and (110) Substrate. *Phys. Rev. B* **2000**, *62*, 8295−8305.

(77) Han, Z.; Tang, C.; Wang, J.; Li, L.; Li, C. Atomically Dispersed Ptn+ Species as Highly Active Sites in Pt/In2O3 Catalysts for Methanol Synthesis from CO2 Hydrogenation. *J. Catal.* **2020**, *394*, 236−244.

(78) Dostagir, N. H. M.; Thompson, C.; Kobayashi, H.; Karim, A. M.; Fukuoka, A.; Shrotri, A. Rh Promoted In2O3 as a Highly Active Catalyst for CO2 Hydrogenation to Methanol. *Catal. Sci. Technol.* **2020**, *10*, 8196−8202.